Medical Engineering and Physics 74 (2019) 73–81

Contents lists available at ScienceDirect

Medical Engineering and Physics

journal homepage: www.elsevier.com/locate/medengphy

Estimation of depth-dependent material properties of biphasic soft tissues through finite element optimization and sensitivity analysis

M. Kerem Ün[a,*], Ahmet Çalık[b]

[a] Department of Biomedical Engineering, Çukurova University, Adana, Turkey
[b] Department of Mechanical Engineering, Mersin University, Mersin, Turkey

ARTICLE INFO

Article history:
Received 5 March 2019
Revised 24 July 2019
Accepted 23 September 2019

Keywords:
Finite element
Optimization
Biphasic
Cartilage
Soft tissue
Depth-dependent
Material property estimation

ABSTRACT

A knowledge of material properties of soft tissue, such as articular cartilage, is essential to assess its mechanical function. It is also increasingly more evident that the inhomogeneity of the tissues plays a significant role in its in vivo functioning. Hence, efficient and reliable tools are needed to accurately characterize the inhomogeneity of the soft tissue mechanical properties. The objective of this research is to propose a finite element optimization procedure to determine depth-dependent material properties of articular cartilage by processing experimental data. Cartilage is modeled as a biphasic continuum with a linear elastic solid phase. The optimization method is based on a sensitivity analysis where the sensitivity of the finite element results to a variation in the material properties is analytically evaluated. The elastic modulus and permeability of the tissue are assumed to vary either linearly or quadratically through the thickness of the cartilage layer. After adopting some initial estimates, these material properties are updated iteratively based on their sensitivities to the current results, and the difference between the actual experimental data and computational experimental data. The optimization method has been tested in two common experimental configurations of cartilage and found to be efficient to estimate the material properties.

1. Introduction

Articular cartilage is a soft connective tissue whose mechanical functions include load-bearing and lubrication in diarthrodial joints. It is a biphasic tissue where the load acting on the joint is mostly carried through the pressurization of the interstitial fluid filling its porous matrix [1]. This structure gives the tissue a time-dependent deformation behavior. In articular cartilage, the direction of the collagen fibers is parallel to the surface in the superficial zone, random in the midzone and perpendicular to the bone interface in the deep zone. As a result, its material properties, especially its elastic modulus, display depth-dependence. A knowledge of cartilage material properties is essential to assess its mechanical function, to better understand the etiology of pathologies like osteoarthritis (OA) and to engineer proper replacement tissue.

The first attempt for measuring depth-dependent properties of cartilage involves epifluorescence microscopy, where depth-dependent elastic modulus, Poisson's ratio and shear modulus [2–6] have been deduced from the equilibrium depth-dependent deformation of the tissue in simple experimental configurations. Inhomogeneity has been also quantified by applying tensile [7], atomic force microscopy [8] and nano-indentation tests [9] to samples harvested from different depth zones of the tissue. These methods rely on equilibrium deformation of cartilage and do not allow the determination of tissue permeability.

Analytical and numerical methods have been utilized to optimize only *homogeneous* material constants of cartilage by matching the relevant experimental data to the available analytical solutions of confined compression (CC) and indentation experiments [1,10]. On the other hand, FE simulations are not restricted to specific experimental configurations, yet they can be as accurate as analytical solutions. Optimization with FE method can be applied in two different ways:

In the first approach, the experiment is simulated with different combinations of the material constants using FE method to form a large set of simulation results (i.e. candidate solutions), where the one matching the experimental output is sought for. *Response Surface* (RS) methodology, *Genetic algorithms* and *artificial neural networks* are such strategies, where the "best" solution is found among the possible candidates. These methods have been used in several studies to predict the homogeneous elastic constants, biphasic poroviscoelastic properties, tissue permeability and

Abbreviations: CC, confined compression; FE, finite element; OA, osteoarthritis; RS, response surface; UCC, unconfined compression.

* Corresponding author.
E-mail address: keremun@cu.edu.tr (M.K. Ün).

https://doi.org/10.1016/j.medengphy.2019.09.019
1350-4533/

orientation distribution of fibers in cartilaginous tissues by simulating either an indentation or unconfined compression (UCC) experiment [11–17].

The second group of FE optimization techniques involve iterative update of material properties through consecutive FE runs until the FE outcome matches the actual experimental outcome. They typically involve a FE package used together with an optimization package. Properties of fibril-reinforced linear and nonlinear poroviscoelastic tissue properties, hyperelastic properties as well as transversely-isotropic properties have been optimized using this approach with varying success in different studies [18–22].

The objective of this study is to propose a finite element (FE) optimization procedure to determine depth-dependent material properties of biphasic tissues. It is shown that this approach can capture inhomogeneous tissue properties in a computationally efficient manner, using experimental data that is obtained through relatively simple experimental means. Linear or quadratic variations are assumed for the elastic modulus and tissue permeability, and the related parameters are optimized with respect to the outcome of the experiment. To achieve that, the sensitivity of the FE results to a variation in the material properties is evaluated as a part of the FE simulation to update the material properties iteratively.

2. Material and methods

Cartilage is modeled as a biphasic continuum and its solid phase is assumed to be linear elastic. (Note that cartilage solid phase behaves linear up to 15% strain [23]. The material properties are updated based on the sensitivities of the FE results to a variation in the material properties is evaluated in a FE-sense as illustrated below. The optimization method has been tested in CC and UCC experimental configurations of cartilage.

2.1. Finite element formulation

We have implemented the *velocity-pressure formulation* (or *vp-formulation*) of the biphasic tissue problem. This formulation has been used for quite some time in cartilage mechanics research. Since the sensitivity analysis presented here uses certain submatrices defined in the FE formulation, we present here the linear vp-formulation involving a linear elastic solid phase. The nonlinear vp-formulation involving a hyperelastic solid phase has been presented elsewhere [24,25].

In the *vp*-formulation, quantities related with the fluid phase are eliminated from the governing equations of the biphasic theory to give the following continuity and momentum equations:

$$\nabla \cdot (\boldsymbol{v} - \kappa \nabla p) = 0 \tag{1}$$

$$\nabla \cdot \left(\boldsymbol{\sigma}^E - p\boldsymbol{I}\right) = \boldsymbol{0} \tag{2}$$

where $\boldsymbol{v}$ is the solid phase velocity, p pressure, $\boldsymbol{\sigma}^E$ elastic stress and κ tissue permeability. Here,"$\nabla\cdot$" is the divergence operator. The following boundary conditions for velocity, pressure and total traction $\boldsymbol{\sigma}^{Tot} = \boldsymbol{\sigma}^E + p\boldsymbol{I}$ are defined on the corresponding boundaries:

$$\boldsymbol{v}^s = \bar{\boldsymbol{v}}^s \quad \text{on } \Gamma_v \tag{3}$$

$$p = \bar{p} \quad \text{on } \Gamma_p \tag{4}$$

$$\boldsymbol{\sigma}^{Tot} \cdot \boldsymbol{n} = \bar{\boldsymbol{t}} \quad \text{on } \Gamma_t \tag{5}$$

where $\bar{\boldsymbol{t}}$ is total applied traction and $\boldsymbol{n}$ indicates the surface normal of the associated boundary.

Eqs. (1), (2) and (5) are multiplied with arbitrary weighting functions, $\boldsymbol{w}$ and q, integrated over the appropriate domains and summed to give:

$$\int_\Omega \left\{\boldsymbol{w} \cdot \left[\nabla \cdot \left(\boldsymbol{\sigma}^E - p\boldsymbol{I}\right)\right] + q[\nabla \cdot (\boldsymbol{v} - \kappa \nabla p)]\right\} + \int_{\Gamma_t} \boldsymbol{w} \cdot \left(\bar{\boldsymbol{t}} - \boldsymbol{\sigma}^{Tot} \cdot \boldsymbol{n}\right) d\Gamma = 0 \tag{6}$$

Using tensorial identities:

$$\int_\Omega \boldsymbol{w} \cdot \left(\nabla \cdot \boldsymbol{\sigma}^E\right) d\Omega = \int_\Omega \nabla \cdot \left(\boldsymbol{\sigma}^E \cdot \boldsymbol{w}\right) d\Omega - \int_\Omega \nabla \boldsymbol{w} : \boldsymbol{\sigma}^E \, d\Omega = \int_{\Gamma_t} \nabla \cdot \left(\boldsymbol{\sigma}^E \cdot \boldsymbol{n}\right) d\Gamma - \int_\Omega \nabla \boldsymbol{w} : \boldsymbol{\sigma}^E \, d\Omega, \tag{7}$$

$$\int_\Omega q \nabla \cdot (\kappa \nabla p) \, d\Omega = \int_{\Gamma_Q} q(\kappa \nabla p) \cdot \boldsymbol{n} \, d\Gamma - \int_\Omega (\kappa \nabla p) \cdot \nabla q d\Omega, \tag{8}$$

$$\int_\Omega \boldsymbol{w} \cdot \nabla p \, d\Omega = \int_{\Gamma_t} p\boldsymbol{w} \cdot \boldsymbol{n} \, d\Gamma - \int_\Omega p \nabla \cdot \boldsymbol{w} \, d\Omega, \tag{9}$$

where **":"** is the double contraction operator, and writing the total traction term as:

$$\int_{\Gamma_t} \boldsymbol{w} \cdot \left(\boldsymbol{\sigma}^{Tot} \cdot \boldsymbol{n}\right) d\Gamma = \int_{\Gamma_t} \boldsymbol{w} \cdot \left(\boldsymbol{\sigma}^E \cdot \boldsymbol{n}\right) d\Gamma - \int_{\Gamma_t} p\boldsymbol{w} \cdot \boldsymbol{n} \, d\Gamma, \tag{10}$$

the final weak form becomes:

$$\int_\Omega \left\{\nabla \boldsymbol{w} : \boldsymbol{\sigma}^E - q \nabla \cdot \boldsymbol{v} - p \nabla \cdot \boldsymbol{w} - \kappa (\nabla p \cdot \nabla q)\right\} d\Omega = \int_{\Gamma_t} \boldsymbol{w} \cdot \bar{\boldsymbol{t}} \, d\Gamma \tag{11}$$

For linear elastic solid phase, $\boldsymbol{\sigma} = \boldsymbol{C}$: $\nabla^{sym}\mathbf{u}$, where $\boldsymbol{C}$ is the fourth-order stiffness tensor and ∇^{sym} is the symmetric gradient operator. Consequently, Eq. (11). can be written as:

$$\int_\Omega \left\{(\nabla \boldsymbol{w})^T : \boldsymbol{C} : \nabla^{sym}\boldsymbol{u} - q \nabla \cdot \boldsymbol{v} - p \nabla \cdot \boldsymbol{w} - \kappa (\nabla p \cdot \nabla q)\right\} d\Omega = \int_{\Gamma_t} \boldsymbol{w} \cdot \bar{\boldsymbol{t}} \, d\Gamma \tag{12}$$

Next, the problem domain is subdivided into tetrahedral "finite elements". With subscript '*e*' indicating the element quantities, the main and weighting variables are interpolated in each element as:

$$\boldsymbol{v}_e = \boldsymbol{N}_e^v \boldsymbol{v}_e^n, \qquad \boldsymbol{u}_e = \boldsymbol{N}_e^v \boldsymbol{u}_e^n, \qquad p_e = \boldsymbol{N}_e^p \boldsymbol{p}_e^n \tag{13}$$

$$\boldsymbol{w}_e = \boldsymbol{N}_e^v \boldsymbol{w}_e^n, \qquad q_e = \boldsymbol{N}_e^p \boldsymbol{q}_e^n \tag{14}$$

where $\boldsymbol{N}_e^v$, $\boldsymbol{N}_e^p$ are the related shape function matrices, and $\boldsymbol{v}_e^n$, $\boldsymbol{u}_e^n$, $\boldsymbol{p}_e^n$, $\boldsymbol{w}_e^n$ and $\boldsymbol{q}_e^n$ are the column vectors containing the associated nodal degrees of freedoms. Velocity and pressure are interpolated with piecewise-quadratic and piecewise-linear functions, respectively. The fourth order tensor $\boldsymbol{C}$ is converted to a 6×6 symmetric matrix and denoted as $\boldsymbol{C}$. Accordingly, the strain matrix is written as a column vector, and the gradient, symmetric gradient and divergence operators are expressed as matrices, denoted by $\mathfrak{L}_{div}$, $\mathfrak{L}_\nabla^{sca}$ and $\mathfrak{L}_\nabla^{sym}$, as:

$$\mathfrak{L}_{div} = \begin{bmatrix} \frac{\partial}{\partial x} & \frac{\partial}{\partial y} & \frac{\partial}{\partial z} \end{bmatrix}, \qquad \mathfrak{L}_\nabla^{sca} = \begin{bmatrix} \frac{\partial}{\partial x} \\ \frac{\partial}{\partial y} \\ \frac{\partial}{\partial z} \end{bmatrix},$$

$$\mathfrak{L}_\nabla^{sym} = \begin{bmatrix} \frac{\partial}{\partial x} & 0 & 0 \\ 0 & \frac{\partial}{\partial y} & 0 \\ 0 & 0 & \frac{\partial}{\partial z} \\ \frac{\partial}{\partial y} & \frac{\partial}{\partial x} & 0 \\ \frac{\partial}{\partial z} & 0 & \frac{\partial}{\partial x} \\ 0 & \frac{\partial}{\partial z} & \frac{\partial}{\partial y} \end{bmatrix} \tag{15}$$

The operators defined above convert some tensorial quantities to their vector forms. With these manipulations, Eq. (13) can be written as,

$$\sum_{e=1}^{nel}\int_{\Omega^e}\left\{\boldsymbol{w}_e^{n^T}\left(L_\nabla^{sym}\boldsymbol{N}_e^v\right)^T\boldsymbol{C}\left(L_\nabla^{sym}\boldsymbol{N}_e^v\right)u_e^n-\boldsymbol{q}_e^{n^T}\boldsymbol{N}_e^{p^T}\left(L_{div}\boldsymbol{N}_e^v\right)\boldsymbol{v}_e^n\right.$$
$$\left.-\boldsymbol{w}_e^{n^T}\left(L_{div}\boldsymbol{N}_e^v\right)^T\boldsymbol{N}_e^p\,\boldsymbol{p}_e^n-\boldsymbol{q}_e^{n^T}\left(L_\nabla^{sca}\boldsymbol{N}_e^p\right)^T\kappa\left(L_\nabla^{sca}\boldsymbol{N}_e^p\right)\boldsymbol{p}_e^n\right\}d\Omega$$
$$=\sum_{e=1}^{nel}\int_{\Gamma_t^e}\boldsymbol{w}_e^{n^T}\boldsymbol{N}_e^{v^T}\bar{\boldsymbol{t}}\,d\Gamma \tag{16}$$

where Ω^e is the element domain. Γ_t^e denote the element faces on the boundary where traction is prescribed. Eq. (16) can be written in the following form:

$$\sum_{e=1}^{nel}\begin{bmatrix}\boldsymbol{w}_e^{n^T} & \boldsymbol{q}_e^{n^T}\end{bmatrix}\left\{\begin{bmatrix}\boldsymbol{0} & -\boldsymbol{A}_{vp}^e\\ -\boldsymbol{A}_{vp}^{e^T} & -\boldsymbol{H}_e\end{bmatrix}\begin{bmatrix}\boldsymbol{v}_e^n\\ \boldsymbol{p}_e^n\end{bmatrix}+\begin{bmatrix}\boldsymbol{K}^{se} & \boldsymbol{0}\\ \boldsymbol{0} & \boldsymbol{0}\end{bmatrix}\begin{bmatrix}\boldsymbol{u}_e^n\\ \boldsymbol{p}_e^n\end{bmatrix}\right\}$$
$$=\sum_{e=1}^{nel}\begin{bmatrix}\boldsymbol{w}_e^{n^T} & \boldsymbol{q}_e^{n^T}\end{bmatrix}\begin{bmatrix}\boldsymbol{F}_t^e\\ \boldsymbol{0}\end{bmatrix} \tag{17}$$

where,

$$\boldsymbol{A}_{vp}^e=\int_{\Omega^e}\left(\mathfrak{L}_{div}\boldsymbol{N}_e^v\right)^T\boldsymbol{N}_e^p\,d\Omega \tag{18}$$

$$\boldsymbol{H}^e=\int_{\Omega^e}\left(\mathfrak{L}_\nabla^{sca}\boldsymbol{N}_e^p\right)^T\kappa\left(\mathfrak{L}_\nabla^{sca}\boldsymbol{N}_e^p\right)d\Omega \tag{19}$$

$$\boldsymbol{K}^{se}=\int_{\Omega^e}\left(\mathfrak{L}_\nabla^{sym}\boldsymbol{N}_e^v\right)^T\boldsymbol{C}\left(\mathfrak{L}_\nabla^{sym}\boldsymbol{N}_e^v\right)d\Omega \tag{20}$$

$$\boldsymbol{F}_t^e=\int_{\Gamma_t^e}\boldsymbol{N}_e^t\bar{\boldsymbol{t}}\,d\Gamma \tag{21}$$

The summations in Eq. (17) are assembled to a global system. Eq. (17) holds for any function taken from weighting function space if:

$$\begin{bmatrix}\boldsymbol{0} & -\boldsymbol{A}_{vp}\\ -\boldsymbol{A}_{vp}^T & -\boldsymbol{H}\end{bmatrix}\begin{bmatrix}\boldsymbol{v}^n\\ \boldsymbol{p}^n\end{bmatrix}+\begin{bmatrix}\boldsymbol{K}^s & \boldsymbol{0}\\ \boldsymbol{0} & \boldsymbol{0}\end{bmatrix}\begin{bmatrix}\boldsymbol{u}^n\\ \boldsymbol{0}\end{bmatrix}=\begin{bmatrix}\boldsymbol{F}_t\\ \boldsymbol{0}\end{bmatrix} \tag{22}$$

The vector and matrices in Eq. (22) are the assembled forms of those in Eq. (17).

Eq. (22) represents a first order differential-algebraic system. We use a Crank-Nicholson scheme to relate the values $\boldsymbol{u}$ and $\boldsymbol{v}$ at the kth and $(k+1)$st time step as:

$$\boldsymbol{u}_{k+1}^n=\left(\omega\,\boldsymbol{v}_{k+1}^n+(1-\omega)\boldsymbol{v}_k^n\right)\Delta t+\boldsymbol{u}_k^n \tag{23}$$

where ω and Δt are the time-integration parameter and time-step size, respectively. Using Eq. (25), Eq. (24) is written as:

$$\begin{bmatrix}\omega\Delta t\boldsymbol{K}^s & -\boldsymbol{A}_{vp}\\ -\boldsymbol{A}_{vp}^T & -\boldsymbol{H}\end{bmatrix}\begin{bmatrix}\boldsymbol{v}_{k+1}^n\\ \boldsymbol{p}_{k+1}^n\end{bmatrix}=\begin{bmatrix}\boldsymbol{F}_t-\boldsymbol{K}^s\left(\boldsymbol{u}_k^n+\boldsymbol{v}_k^n(1-\omega)\Delta t\right)\\ \boldsymbol{0}\end{bmatrix} \tag{24}$$

In the above equation, the solution at the kth time step is used to update the right hand side. The system is solved with the updated right hand side to obtain the solution of the next $(k+1)$st time step.

2.2. Optimization

FE simulation of biphasic tissue with known material properties is mathematically a *forward problem*. On the other hand, determination of biphasic properties from a given set of experimental observations constitutes an *inverse problem*. Forward problems are usually well-conditioned. However, inverse problems are mathematically ill-conditioned, in general, where a small change in the problem input (i.e. experimental data) may create a disproportionally large change in the output. Usually, some *regularization* (i.e. a set of constraints) has to be applied to find a solution to the inverse problem.

Let $\boldsymbol{m}$ and $\boldsymbol{y}$ denote the column vectors containing the experimental data items and the corresponding FE output items, respectively. $\boldsymbol{y}$ is a function of the material properties, i.e.:

$$\boldsymbol{y}=\boldsymbol{y}(\boldsymbol{\theta}) \tag{25}$$

where $\boldsymbol{\theta}$ is the vector containing the material properties to be optimized. The objective function to be minimized can be expressed as

$$f=f(\boldsymbol{m},\boldsymbol{y}(\boldsymbol{\theta}),\boldsymbol{\theta}) \tag{26}$$

The functional relation between $\boldsymbol{y}$ and $\boldsymbol{\theta}$ is generally nonlinear independent of the linearity of the underlying physical problem. Consequently, an iterative scheme is necessary to estimate the material properties by minimizing f.

Since the material properties are continuous quantities, we have employed a *gradient* optimization method, where the gradient of the objective function with respect to the properties $\boldsymbol{\theta}$ needs to be calculated.

The objective function J involves the difference-squares between the experimental and the related FE outcome:

$$J=(\boldsymbol{m}-\boldsymbol{y}(\boldsymbol{\theta}))^T\boldsymbol{Q}(\boldsymbol{m}-\boldsymbol{y}(\boldsymbol{\theta})) \tag{27}$$

Depending on what is measured in the experiment, the vector $\boldsymbol{m}$ may contain quantities of different nature/scale (such as pressure and displacement) simultaneously and the matrix $\boldsymbol{Q}$ is used to make these quantities non-dimensional such that their errors can be added. In this work, our virtual experimental data contains only displacement quantities since displacement is the typical quantity to be measured in cartilage experimentation. $\boldsymbol{Q}$ can be taken as the identity matrix. Hence, Eq. (29) can be written as:

$$J=(\boldsymbol{m}-\boldsymbol{y}(\boldsymbol{\theta}))^T(\boldsymbol{m}-\boldsymbol{y}(\boldsymbol{\theta})) \tag{28}$$

To find the extremum of the objective function, its variation is evaluated with respect to an infinitesimal change $\delta\boldsymbol{\theta}$ in the material properties and set to zero. The variations of Eq. (28) can be expressed as:

$$\delta J=(\delta\boldsymbol{y}(\boldsymbol{\theta}))^T(\boldsymbol{m}-\boldsymbol{y})+(\boldsymbol{m}-\boldsymbol{y})^T(\delta\boldsymbol{y}(\boldsymbol{\theta}))=0 \tag{29}$$

The variation of $\boldsymbol{y}$, $\delta\boldsymbol{y}$, can be written as:

$$\delta\boldsymbol{y}(\boldsymbol{\theta})=\frac{\partial\boldsymbol{y}(\boldsymbol{\theta})}{\partial\boldsymbol{\theta}}\delta\boldsymbol{\theta}=\boldsymbol{S}\delta\boldsymbol{\theta}. \tag{30}$$

where $\boldsymbol{S}=\frac{\partial\boldsymbol{y}(\boldsymbol{\theta})}{\partial\boldsymbol{\theta}}$ is the *sensitivity matrix* describing the change in the FEM output $\boldsymbol{y}$ with respect to a change in $\boldsymbol{\theta}$. In biphasic analysis, variation in a specific material constant may change the outcome measured at different geometry points and analysis times differently. A higher change in the outcome means a higher sensitivity of the outcome at the considered point/time to the considered material constant.

Introducing Eq. (30) into Eq. (29) gives

$$\delta J=(\boldsymbol{S}\delta\boldsymbol{\theta})^T(\boldsymbol{m}-\boldsymbol{y}(\boldsymbol{\theta}))+(\boldsymbol{m}-\boldsymbol{y}(\boldsymbol{\theta}))^T(\boldsymbol{S}\delta\boldsymbol{\theta})=0 \tag{31}$$

The matrix products in Eq. (31) are scalars of equal value. Hence:

$$\delta J=\delta\boldsymbol{\theta}^T\boldsymbol{S}^T(\boldsymbol{m}-\boldsymbol{y}(\boldsymbol{\theta}))=0. \tag{32}$$

Since $\delta\boldsymbol{\theta}$ is arbitrary, the above equation holds only if

$$r(\boldsymbol{\theta})=\boldsymbol{S}^T(\boldsymbol{m}-\boldsymbol{y}(\boldsymbol{\theta}))=0. \tag{33}$$

Denoting this expression as the residual $\boldsymbol{r}(\boldsymbol{\theta})$, Eq. (33) is a nonlinear equation system with the unknown $\boldsymbol{\theta}$. The system is solved

using the Newton–Raphson iteration. To achieve that, it is linearized at a reference material property state $\boldsymbol{\theta} = \boldsymbol{\theta}^l$ as:

$$\left.\frac{\partial \boldsymbol{r}}{\partial \boldsymbol{\theta}}\right|_{\boldsymbol{\theta}=\boldsymbol{\theta}^l} \delta\boldsymbol{\theta}^{l+1} = -\boldsymbol{r}(\boldsymbol{\theta}^l). \tag{34}$$

$\boldsymbol{\theta}^l$ indicates the material property estimate from the previous iteration. The solution $\delta\boldsymbol{\theta}^{l+1}$ is the correction to the current estimate $\boldsymbol{\theta}^l$. If the process is convergent, the norm of the right hand side vector $-\mathbf{r}(\boldsymbol{\theta}^l)$ should eventually vanish.

Differentiating Eq. (33) with respect to $\boldsymbol{\theta}$ gives

$$\frac{\partial \boldsymbol{r}(\boldsymbol{\theta})}{\partial \boldsymbol{\theta}} = (\boldsymbol{S}^l)^T\left(-\frac{\partial \boldsymbol{y}}{\partial \boldsymbol{\theta}}\right) + \frac{\partial (\boldsymbol{S}^T)^l}{\partial \boldsymbol{\theta}}(\boldsymbol{m} - \boldsymbol{y}(\boldsymbol{\theta})^l) \tag{35}$$

Recalling that $\boldsymbol{S} = \frac{\partial \boldsymbol{y}}{\partial \boldsymbol{\theta}}$ by definition, Eq. (35) can be written as:

$$\frac{\partial \boldsymbol{r}(\boldsymbol{\theta})}{\partial \boldsymbol{\theta}} = (\boldsymbol{S}^l)^T\boldsymbol{S}^l + \frac{\partial (\boldsymbol{S}^T)^l}{\partial \boldsymbol{\theta}}(\boldsymbol{m} - \boldsymbol{y}(\boldsymbol{\theta})^l) \tag{36}$$

$\frac{\partial \boldsymbol{S}^l}{\partial \boldsymbol{\theta}}$ is a second order term and ignored to simplify computation. In other words, rather than the exact gradient, an approximate gradient of $\boldsymbol{r}$ is calculated. Since the scheme represented in Eq. (34) is iterative, ignoring this term is not a problem as long as the right hand side $-\mathbf{r}(\boldsymbol{\theta}^l)$ is exact. With this consideration, the linearized system of Eq. (34) can be written as

$$\left[(\boldsymbol{S}^l)^T\boldsymbol{S}^l\right](\delta\boldsymbol{\theta}^{l+1}) = -(\boldsymbol{S}^l)^T(\boldsymbol{m} - \boldsymbol{y}(\boldsymbol{\theta})^l) \tag{37}$$

Once the above square system is solved, the current estimate for material properties is updated as

$$\boldsymbol{\theta}^{l+1} = \boldsymbol{\theta}^l + \delta\boldsymbol{\theta}^{l+1} \tag{38}$$

and the procedure is repeated.

2.3. Sensitivity analysis based on finite element formulation

While the gradient optimization scheme described above is general, the sensitivity matrix $\boldsymbol{S}$ is very much problem-dependent.

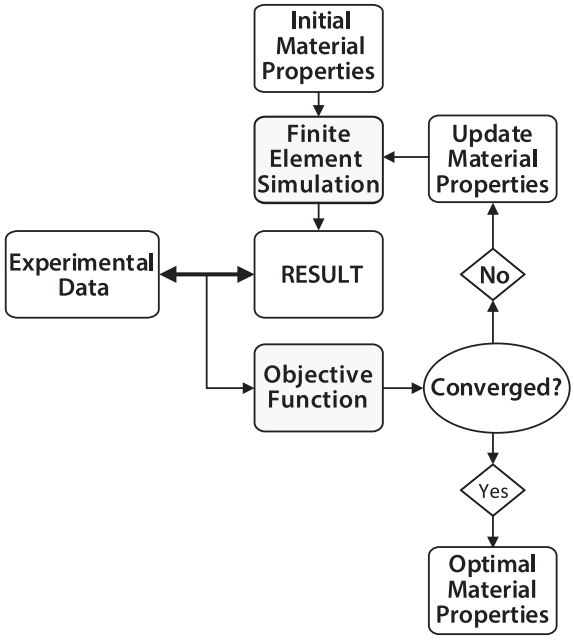

Fig. 1. Flowchart of the optimization algorithm. The experiment is simulated with FE and its results are compared with experimental data. Material properties are updated, and simulation is repeated until simulation results matches the experimental data.

In this section, we demonstrate how to derive the sensitivity matrix $\boldsymbol{S}$ in connection with the *vp*-formulation given in Eq. (24).

A variation $\delta\boldsymbol{\theta}$ in the material properties will cause a change in the vectors $\boldsymbol{v}$, $\boldsymbol{u}$ and $\boldsymbol{p}$ and matrices $\boldsymbol{K}$ and $\boldsymbol{H}$ in Eq. (22). Consequently, the variation in Eq. (22) can be written as

$$\begin{aligned} -\boldsymbol{A}\delta\boldsymbol{p}^n + \boldsymbol{K}\delta\boldsymbol{u}^n + \delta\boldsymbol{K}\boldsymbol{u}^n &= \boldsymbol{0} \\ -\boldsymbol{A}^T\delta\boldsymbol{v}^n - \boldsymbol{H}\delta\boldsymbol{p}^n - \delta\boldsymbol{H}\boldsymbol{p}^n &= \boldsymbol{0} \end{aligned} \tag{39}$$

The unknown sensitivities of the problem variables $\boldsymbol{v}$, $\boldsymbol{u}$ and $\boldsymbol{p}$ to the material properties $\boldsymbol{\theta}$ are also interpolated using the same

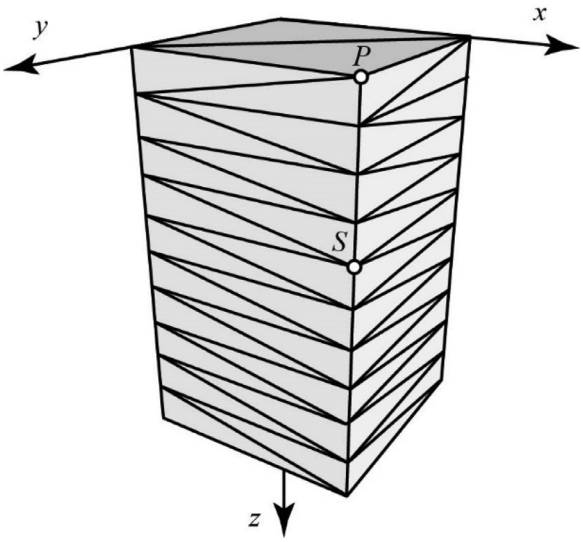

Fig. 2. FE mesh for CC creep test.

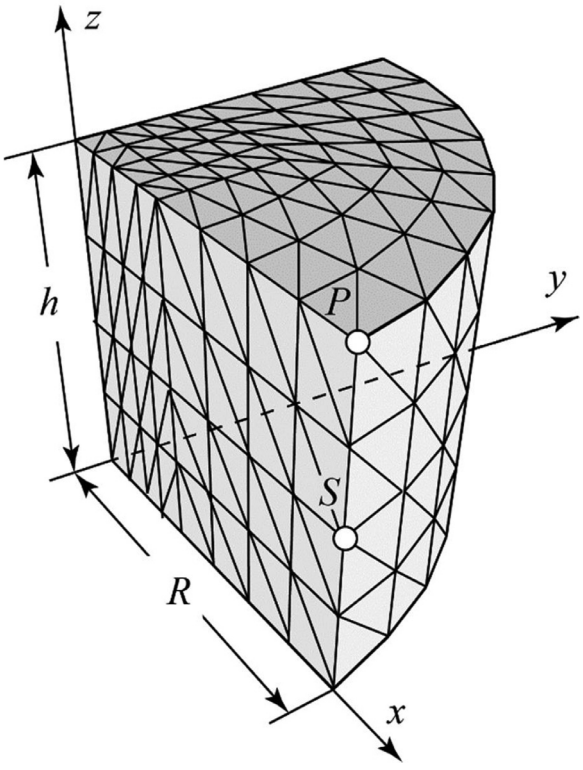

Fig. 3. FE mesh for UCC test.

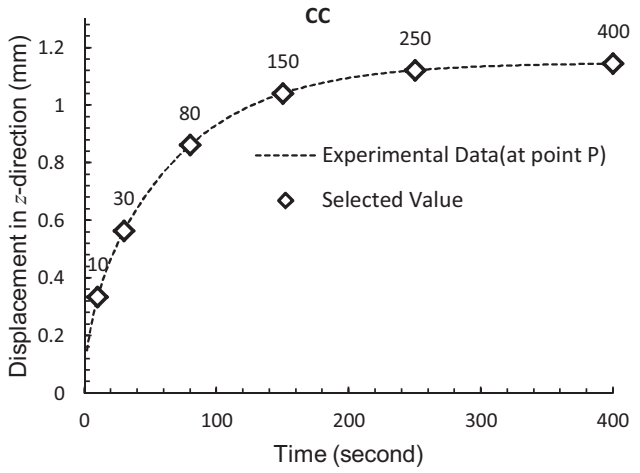

Fig. 4. The result of the simulated CC experiment with linearly varying properties and the experimental data selected to be used in optimization.

functions. Their nodal vectors can be defined as:

$$\delta \boldsymbol{v}^n = \boldsymbol{V}^n \delta\boldsymbol{\theta}, \quad \delta \boldsymbol{u}^n = \boldsymbol{U}^n \delta\boldsymbol{\theta}, \quad \delta \boldsymbol{p}^n = \boldsymbol{P}^n \delta\boldsymbol{\theta} \tag{40}$$

where $\boldsymbol{V}^n$, $\boldsymbol{U}^n$ and $\boldsymbol{P}^n$ are the element sensitivity matrices of these variables. Each column in these matrices represent the sensitivity of all nodal results with respect to a specific material constant. Hence, these matrices possess as many columns as there are material properties to be optimized in $\boldsymbol{\theta}$. Variations in $\boldsymbol{K}$ and $\boldsymbol{H}$ are expressed as:

$$\delta \boldsymbol{K} = \frac{\partial \boldsymbol{K}}{\partial \boldsymbol{\theta}} \delta\boldsymbol{\theta}, \quad \delta \boldsymbol{H} = \frac{\partial \boldsymbol{H}}{\partial \boldsymbol{\theta}} \delta\boldsymbol{\theta} \tag{41}$$

Substituting Eqs. (40) and (41) into Eq. (39), and rearranging gives

$$\left[\boldsymbol{A}\boldsymbol{P}^n + \boldsymbol{K}\boldsymbol{U}^n + \frac{\partial \boldsymbol{K}}{\partial \boldsymbol{\theta}}\boldsymbol{u}^n\right]\delta\boldsymbol{\theta} = \boldsymbol{0}$$
$$\left[-\boldsymbol{A}^T\boldsymbol{V}^n - \boldsymbol{H}\boldsymbol{P}^n - \frac{\partial \boldsymbol{H}}{\partial \boldsymbol{\theta}}\boldsymbol{p}^n\right]\delta\boldsymbol{\theta} = \boldsymbol{0} \tag{42}$$

Since $\delta\boldsymbol{\theta}$ is arbitrary, the expressions in the brackets must vanish, resulting to the following system:

$$\begin{bmatrix} \boldsymbol{0} & -\boldsymbol{A} \\ -\boldsymbol{A}^T & -\boldsymbol{H} \end{bmatrix}\begin{bmatrix} \boldsymbol{V}^n \\ \boldsymbol{P}^n \end{bmatrix} + \begin{bmatrix} \boldsymbol{K} & \boldsymbol{0} \\ \boldsymbol{0} & \boldsymbol{0} \end{bmatrix}\begin{bmatrix} \boldsymbol{U}^n \\ \boldsymbol{0} \end{bmatrix} = \begin{bmatrix} -\frac{\partial \boldsymbol{K}}{\partial \boldsymbol{\theta}}\boldsymbol{u}^n \\ \frac{\partial \boldsymbol{H}}{\partial \boldsymbol{\theta}}\boldsymbol{p}^n \end{bmatrix} \tag{43}$$

If the Crank-Nicholson scheme (Eq. (23)) is applied to Eq. (43) we obtain:

$$\begin{bmatrix} \omega\Delta t\boldsymbol{K}(\boldsymbol{\theta}) & -\boldsymbol{A} \\ -\boldsymbol{A}^T & -\boldsymbol{H}(\boldsymbol{\theta}) \end{bmatrix}\begin{bmatrix} \boldsymbol{V}_{k+1}^n \\ \boldsymbol{P}_{k+1}^n \end{bmatrix} = \begin{bmatrix} -\frac{\partial \boldsymbol{K}}{\partial \theta}\boldsymbol{u}_{k+1}^n - \boldsymbol{K}(\boldsymbol{\theta})\left(\boldsymbol{V}_k^n + \boldsymbol{V}_k^n(1-\omega)\Delta t\right) \\ \frac{\partial \boldsymbol{H}}{\partial \theta}\boldsymbol{p}_{k+1}^n \end{bmatrix} \tag{44}$$

The above system has the same coefficient matrix as in Eq. (24) but a different right hand side. Hence, the sensitivities can be calculated during the FE simulation without forming a separate global system by solving the same system with a different right hand side. Consequently, the computational load of the sensitivity problem amounts merely to a few extra back-substitutions in the FE analysis.

The right hand side of Eq. (44) is calculated using the FE solution of $(k+1)$st time step and the sensitivities of the kth time step. The solution of Eq. (44) with each column of the right hand side will produce one column of $\boldsymbol{V}_{k+1}^n$ and $\boldsymbol{P}_{k+1}^n$(and then $\boldsymbol{U}_{k+1}^n$). The sensitivity matrix $\boldsymbol{S}$ is then formed with the entries of $\boldsymbol{V}^n$, $\boldsymbol{P}^n$ and $\boldsymbol{U}^n$ corresponding to the experimental output points and times.

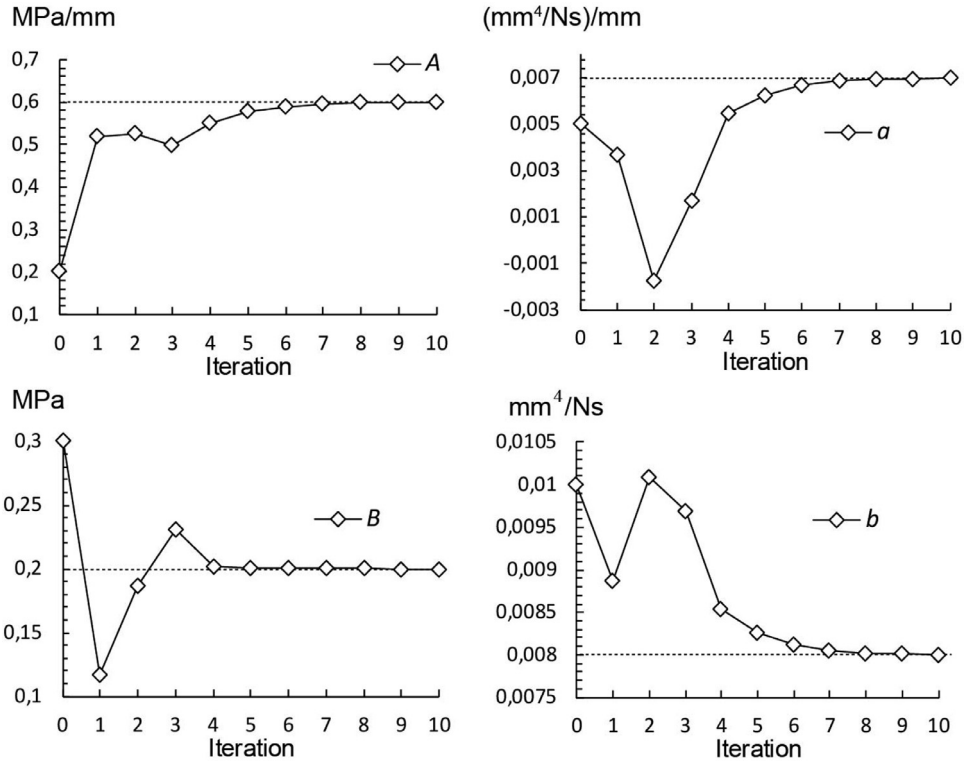

Fig. 5. The evolution of the constants A and B (related to E), and a and b (related to κ) during optimization iteration in CC test.

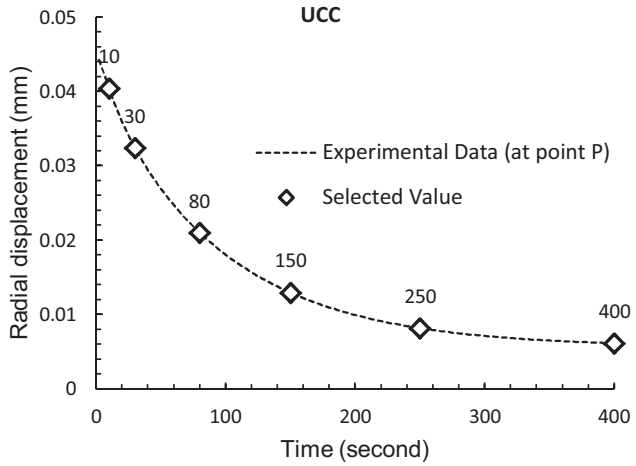

Fig. 6. The result of the simulated UCC experiment with linearly varying properties and the experimental data selected to be used in optimization.

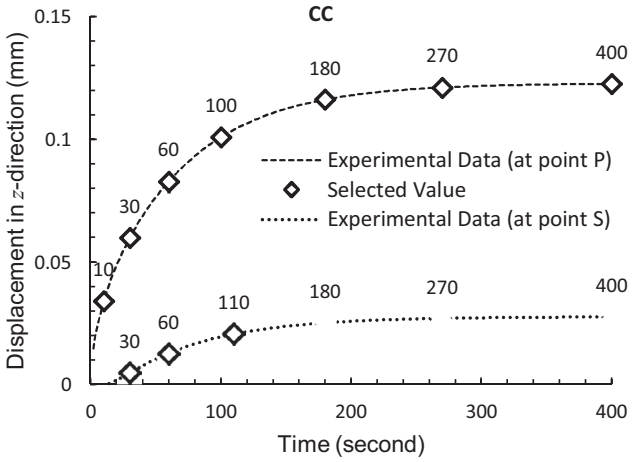

Fig. 8. The result of the simulated CC experiment with quadratically varying properties and the experimental data selected to be used in optimization.

2.4. Programming

The optimization scheme involving the sensitivity analysis and the FE program has been coded in MATLAB environment. A variety of tests have been applied to validate the developed FE code. In particular, the results have been compared with the available analytical solutions for CC and UCC [26] configurations. Furthermore, the same problems with homogeneous properties have been setup in ANSYS (Ansys Inc., USA) and FeBio (Musculoskeletal Research Laboratories, University of Utah, USA) packages and their outcome has been compared with ours.

The optimization algorithm is schematically depicted on Fig. 1.

3. Example problems and results

3.1. Experimental configurations and creation of virtual experimental data

We have tested the optimization scheme with virtual CC (Fig 2.) and UCC (Fig. 3) creep experiments [23]. Either linearly or quadratically varying material properties across the tissue depth have been assumed. The contact between the tissue and experimental platens is assumed to be frictionless. The CC and UCC meshes have 273 and 1953 nodes, respectively, and it has been observed that convergent solutions could be obtained on both meshes. Both meshes

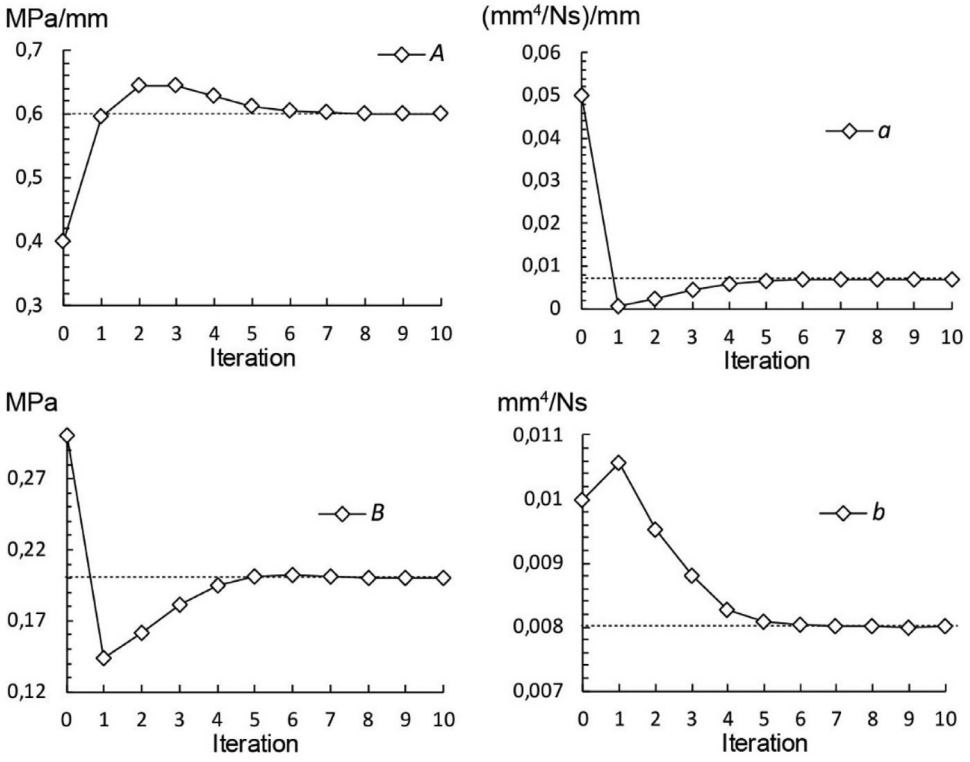

Fig. 7. The evolution of the constants A and B (related to E), and a and b (related to κ) during optimization iteration in UCC test.

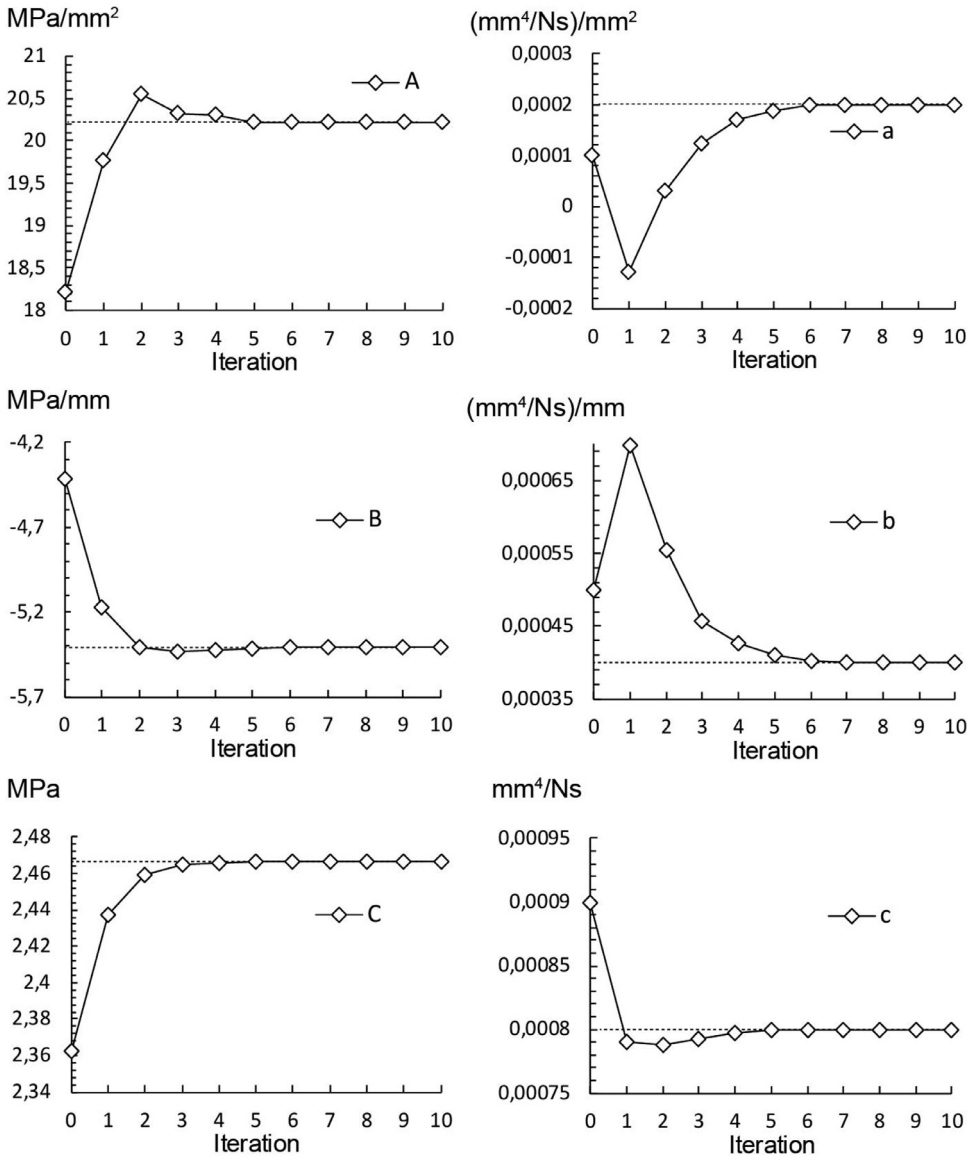

Fig. 9. The evolution of the constants A, B and C (related to E), and a, b and c (related to κ) during optimization iteration in CC test.

represent a tissue of thickness $h = 1$ mm. For simplicity, E and κ have been assumed to be depth-dependent while ν is taken to be homogeneous and equal to $\nu = 0.05$.

In engineering analysis involving a forward and inverse problem pair, it is common practice to test the inverse analysis using "experimental data" created with the forward analysis [17,22,27,28], and a similar approach has been used here, too. First, the FE code (i.e. the forward problem) is run with a specific set of depth-dependent material properties, whose outcome at selected nodes and times is taken as virtual experimental data. The optimization code is then run and checked if it can predict these depth-dependent material properties that have been used in the creation of the virtual experimental data.

3.2. Results with linearly varying material properties

The elastic modulus has been observed to have a linear variation across the tissue depth in some studies [9]. Hence, as the first test problem, we have assumed properties that vary linearly with depth z:

$$E = Az + B \tag{45}$$

$$\kappa = az + b \tag{46}$$

where A, B, a and b are the material constants to be optimized. To create the virtual experimental data for CC and UCC, the FE code is run with the following physiologically realistic numerical forms:

$$E = 0.6z + 0.2 \quad \text{MPa} \tag{47}$$

$$\kappa = 0.007z + 0.008 \quad \text{mm}^4/\text{Ns} \tag{48}$$

In other words, the optimization scheme, if successful, should predict the values $A = 0.6$ MPa/mm, $B = 0.2$ MPa, $a = 0.007$ mm^4/Ns/mm and $b = 0.008$ mm^4/Ns.

We have taken axial displacements measured at Point P (Fig. 2.) at six different times (at 10, 30, 80, 150, 250 and 400 s) as our experimental data for the virtual CC experiment (Fig. 4).

The optimization scheme is started with initial estimates of material constants that differ significantly from their actual values. The scheme has been observed to capture the correct values of *A, B, a* and *b* in eight iterations, i.e. after eight material property updates and FE reruns (Fig. 5.).

As the data of UCC experiment, we have picked the radial displacement values at Point P (Fig. 3) at, again, 10, 30, 80, 150, 250 and 400 s (Fig. 6). In this problem, *A, B, a* and *b* have converged to their actual values in about eight iterations (Fig. 7).

3.3. Results with quadratically varying material properties

In some studies, material properties of articular cartilage have been observed to vary quadratically with tissue depth [2,29], which can be expressed as:

$$E = Az^2 + Bz + C \quad \text{MPa} \tag{49}$$

$$\kappa = az^2 + bz + c \quad \text{mm}^4/\text{Ns} \tag{50}$$

In this case, the material properties to be optimized are *A, B, C, a, b* and *c*. To create the virtual experimental data, we have adopted the data given by Kahn et al. [29] for E to a quadratic distribution and assumed a physiologically meaningful distribution for κ as:

$$E = 20.21z^2 - 5.41z + 2.47 \quad \text{MPa} \tag{51}$$

$$\kappa = 0.0002z^2 + 0.0004z + 0.0008 \quad \text{mm}^4/\text{Ns} \tag{52}$$

Hence, the material properties that are to be predicted by the optimization scheme are $A = 20.21\ \text{MPa/mm}^2$, $B = -5.410\ \text{MPa/mm}$, $C = 2.466\ \text{MPa}$, $a = 0.0002\ \text{mm}^4/\text{Ns/mm}^2$, $b = 0.0004\ \text{mm}^4/\text{Ns/mm}$ and $c = 2.466\ \text{mm}^4/\text{Ns}$. From the simulated CC experiment, we have picked axial displacements at Points P and S (Fig. 2) at 13 different times (at 10, 30, 60, 100, 180, 270 and 400 s for P, and 30, 60, 110, 180, 270 and 400 s for S) as our experimental data (Fig. 8). The material properties have converged to their actual values in about six iterations in this problem (Fig. 9).

A similar analysis performed with the UCC experiment by taking the radial displacement values at two measurement points P and S (Fig. 3) at 13 different times yields results similar to CC experiment and not reported here for brevity.

4. Discussion and conclusion

To the best of our knowledge, the work presented here is the first study where a sensitivity-based FE scheme is utilized to determine inhomogeneous (or even homogeneous) properties of linear elastic cartilage. Although algorithmic details are omitted, only one previous work involves a quasi-Newton sensitivity calculation to optimize homogeneous properties [18].

In the literature, inhomogeneous elastic properties have been usually measured from the equilibrium tissue deformation by employing advanced visualization techniques (e.g. epifluoroscopy) or sophisticated mechanical experiments (e.g. nanoindentation). On the other hand, our algorithm can predict simultaneously the elastic modulus and the permeability of the tissue. Moreover, in the case of linear variation across the depth, the inhomogeneity of both properties are estimated using displacement measurements taken only at the tissue surface in both CC and UCC configurations. Considering that the surface displacement of the biphasic tissue is relatively easy to measure in an experiment, sensitivity-based optimization has the potential to capture inhomogeneous properties through more basic experimentation performed on biphasic tissues. We believe this point to be the major strength of the presented approach.

The presented scheme is computationally efficient since sensitivities are calculated from the available matrices of the FE formulation during the FE simulation. Existing FE methods that do not involve any sensitivity analysis (RS, genetic algorithms etc.) require a large set of candidate solutions that is created by running FE analyses sometimes hundreds of times with different material property combinations [11–13,15,16,30], whereas our scheme converges to correct properties in 6–8 FE runs. Furthermore, these studies usually employ ready FE packages, which makes it impossible/difficult to manipulate the FE formulation or impose inhomogeneity in a functional form the way it is done in the current work.

The presented method has the potential to capture the biphasic material properties, if they can be expressed in simple functional forms. In practice, the material property distribution in a biological tissue will not have an exact functional form. If the method is applied to actual experimental data with an assumption of, say, linear distribution, then the algorithm will retrieve the “best” linear distribution that represents the tissue behavior. In this case, there will be no “perfect match” to the material properties and the error norm between the actual and virtual experiment outcomes will not decrease beyond a minimum value.

Theoretically, two different set of material property distributions can produce the same experimental data at the selected experimental data points/times. Multiple solutions is a characteristics of many inverse problems. By assuming a certain functional form for a material constant, the solution is constraint and the possibility of multiple solutions is eliminated; i.e. the ill-posed inverse problem is regularized.

The optimization scheme has been tested successfully both in CC and UCC geometries in the case of linearly varying depth-dependent properties. The case of quadratically-varying properties involve a larger number properties to be optimized. Consequently, for convergence, more experimental data items, and better initial estimates are required in this case. Nevertheless, we have observed that the convergence performance of the scheme can be improved by including experimental data items measured at diverse points/times in the analysis.

The main motivation of material property estimation studies for soft tissues have been sofar to better understand their mechanical functions and the etiology of related pathologies such as OA. In the future, such studies may form the basis of new diagnosis tools. For instance, efforts already exist to correlate the likelihood of skin cancer to the mechanical properties of the skin [31]. Similarly, cancers of brain, breast and prostate are known to change the mechanical properties of the tissue [32–34]. Skin and brain (among others) are soft tissues known to behave biphasic and biphasic models, applied to these tissues, may produce a distinction between the properties of healthy and pathologic tissues.

Articular cartilage is known to behave nonlinearly both under in vivo and in vitro conditions. Accordingly, a work in progress is the extension of the sensitivity analysis to predict hyperelastic properties, strain-dependent permeability and any possible related inhomogeneities of the tissue.

Funding

None.

Ethical approval

Not required.

Declaration of Competing Interest

None declared.

References

[1] Mow VC, Gibbs MC, Lai WM, Zhu WB, Athanasiou KA. Biphasic indentation of articular cartilage—II. A numerical algorithm and an experimental study. J Biomech 1989;22:853–61. doi:10.1016/0021-9290(89)90069-9.

[2] Schinagl RM, Gurskis D, Chen AC, Sah RL. Depth-dependent confined compression modulus of full-thickness bovine articular cartilage. J Orthop Res 1997;15:499–506. doi:10.1002/jor.1100150404.

[3] Wang CC-B, Deng J-M, Ateshian GA, Hung CT. An automated approach for direct measurement of two-dimensional strain distributions within articular cartilage under unconfined compression. J Biomech Eng 2002;124:557. doi:10.1115/1.1503795.

[4] Klein TJ, Chaudhry M, Bae WC, Sah RL. Depth-dependent biomechanical and biochemical properties of fetal, newborn, and tissue-engineered articular cartilage. J Biomech 2007;40:182–90. doi:10.1016/j.jbiomech.2005.11.002.

[5] Buckley MR, Gleghorn JP, Bonassar LJ, Cohen I. Mapping the depth dependence of shear properties in articular cartilage. J Biomech 2008;41:2430–7. doi:10.1016/j.jbiomech.2008.05.021.

[6] Silverberg JL, Dillavou S, Bonassar L, Cohen I. Anatomic variation of depth-dependent mechanical properties in neonatal bovine articular cartilage. J Orthop Res 2013;31:686–91. doi:10.1002/jor.22303.

[7] Charlebois M, McKee MD, Buschmann MD. Nonlinear tensile properties of bovine articular cartilage and their variation with age and depth. J Biomech Eng 2004;126:129. doi:10.1115/1.1688771.

[8] McLeod MA, Wilusz RE, Guilak F. Depth-dependent anisotropy of the micromechanical properties of the extracellular and pericellular matrices of articular cartilage evaluated via atomic force microscopy. J Biomech 2013;46:586–92. doi:10.1016/j.jbiomech.2012.09.003.

[9] Antons J, Marascio MGM, Nohava J, Martin R, Applegate LA, Bourban PE, et al. Zone-dependent mechanical properties of human articular cartilage obtained by indentation measurements. J Mater Sci Mater Med 2018;29. doi:10.1007/s10856-018-6066-0.

[10] Best BA, Guilak F, Setton LA, Zhu W, Saed-Nejad F, Ratcliffe A, et al. Compressive mechanical properties of the human anulus fibrosus and their relationship to biochemical composition. Spine (Phila Pa 1976) 1994;19:212–21. doi:10.1097/00007632-199401001-00017.

[11] Keenan KEKE, Kourtis LCLC, Besier TFTF, Lindsey DPDP, Gold GEGE, Delp SLSL, et al. New resource for the computation of cartilage biphasic material properties with the interpolant response surface method. Comput Methods Biomech Biomed Engin 2009;12:415–22. doi:10.1080/10255840802654319.

[12] Gupta S, Lin J, Ashby P, Pruitt L. A fiber reinforced poroelastic model of nanoindentation of porcine costal cartilage: a combined experimental and finite element approach. J Mech Behav Biomed Mater 2009;2:326–38. doi:10.1016/j.jmbbm.2008.09.003.

[13] Miller GJ, Morgan EF. Use of microindentation to characterize the mechanical properties of articular cartilage: comparison of biphasic material properties across length scales. Osteoarthr Cartil 2010;18:1051–7. doi:10.1016/j.joca.2010.04.007.

[14] Nikkhoo M, Hsu Y-C, Haghpanahi M, Parnianpour M, Wang J-L. A meta-model analysis of a finite element simulation for defining poroelastic properties of intervertebral discs. Proc Inst Mech Eng Part H J Eng Med 2013;227:672–82. doi:10.1177/0954411913480668.

[15] Cao L, Youn I, Guilak F, Setton LA. Compressive properties of mouse articular cartilage determined in a novel micro-indentation test method and biphasic finite element model. J Biomech Eng 2006;128:766. doi:10.1115/1.2246237.

[16] Olberding JE, Francis Suh J-K. A dual optimization method for the material parameter identification of a biphasic poroviscoelastic hydrogel: potential application to hypercompliant soft tissues. J Biomech 2006;39:2468–75. doi:10.1016/j.jbiomech.2005.07.019.

[17] Arbabi V, Pouran B, Campoli G, Weinans H, Zadpoor AA. Determination of the mechanical and physical properties of cartilage by coupling poroelastic-based finite element models of indentation with artificial neural networks. J Biomech 2016;49:631–7. doi:10.1016/j.jbiomech.2015.12.014.

[18] Athanasiou KA, Agarwal A, Muffoletto A, Dzida FJ, Constantinides G, Clem M. Biomechanical properties of hip cartilage in experimental animal models. Clin Orthop Relat Res 1995:254–66 NA. doi:10.1097/00003086-199507000-00035.

[19] Lei F, Szeri AZ. Inverse analysis of constitutive models: biological soft tissues. J Biomech 2007;40:936–40. doi:10.1016/j.jbiomech.2006.03.014.

[20] Seifzadeh A, Oguamanam DCD, Trutiak N, Hurtig M, Papini M. Determination of nonlinear fibre-reinforced biphasic poroviscoelastic constitutive parameters of articular cartilage using stress relaxation indentation testing and an optimizing finite element analysis. Comput Methods Programs Biomed 2012;107:315–26. doi:10.1016/j.cmpb.2011.07.004.

[21] Chung C-Y, Mansour JM. Determination of poroelastic properties of cartilage using constrained optimization coupled with finite element analysis. J Mech Behav Biomed Mater 2015;42:10–18. doi:10.1016/j.jmbbm.2014.10.007.

[22] Op den Camp OMGC, Oomens CWJ, Veldpaus FE, Janssen JD. An efficient algorithm to estimate material parameters of biphasic mixtures. Int J Numer Methods Eng 1999;45:1315–31 9<1315::AID-NME633>3.0.CO;2-A. doi:10.1002/(SICI)1097-0207(19990730)45.

[23] Mow VC, Gu WY, Chen FH. Structure and function of articular cartilage and meniscus. Basic Orthop. Biomech. Mechano-biology 2005. doi:10.1007/978-1-4614-1704-0.

[24] Almeida ES, Spilker RL. Mixed and penalty finite element models for the nonlinear behavior of biphasic soft tissues in finite deformation: part I - alternate formulations. Comput Methods Biomech Biomed Engin 1997;1:25–46. doi:10.1080/01495739708936693.

[25] Ün K, Spilker RL. A penetration-based finite element method for hyperelastic 3D biphasic tissues in contact. part II: finite element simulations. J Biomech Eng 2006;128:934. doi:10.1115/1.2354203.

[26] Armstrong CG, Lai WM, Mow VC. An analysis of the unconfined compression of articular cartilage. J Biomech Eng 1984;106:165–73. doi:10.1115/1.3138475.

[27] Wilke D, Kok S, Heymann G. Comparison of two inverse strategies to characterise soil profiles. Eng. Optim. 2014 2014. doi:10.1201/b17488-182.

[28] Nielsen BF, Lysaker M, Tveito A. On the use of the resting potential and level set methods for identifying ischemic heart disease: an inverse problem. J Comput Phys 2007;220:772–90. doi:10.1016/j.jcp.2006.05.040.

[29] Kahn D, Les C, Xia Y. Effects of cryopreservation on the depth-dependent elastic modulus in articular cartilage and implications for osteochondral grafting. J Biomech Eng 2015;137:1–6. doi:10.1115/1.4029182.

[30] Gohari E, Nikkhoo M, Haghpanahi M, Parnianpour M. Analysis of different material theories used in a FE model of a lumbar segment motion. Acta Bioeng Biomech 2013;15:33–41. doi:10.5277/abb130204.

[31] Dagdeviren C, Su Y, Joe P, Yona R, Liu Y, Kim YS, et al. Conformable amplified lead zirconate titanate sensors with enhanced piezoelectric response for cutaneous pressure monitoring. Nat Commun 2014. doi:10.1038/ncomms5496.

[32] Good DW, Stewart GD, Hammer S, Scanlan P, Shu W, Phipps S, et al. Elasticity as a biomarker for prostate cancer: a systematic review. BJU Int 2014. doi:10.1111/bju.12236.

[33] Hoyt K, Castaneda B, Zhang M, Nigwekar P, di Sant'Agnese PA, Joseph JV, et al. Tissue elasticity properties as biomarkers for prostate cancer. Cancer Biomarkers 2008. doi:10.3233/CBM-2008-44-505.

[34] Zheng YP, Huang YP. Measurement of soft tissue elasticity in vivo: techniques and applications; 2016.